1
Properties of Carbon: An Overview

Shengxi Huang, Johan Ek Weis, Sara Costa, Martin Kalbac, and Mildred S. Dresselhaus

1.1
Overview of Properties

Carbon (element No. 6 in the periodic table) forms a variety of materials, including graphite, diamond, carbon fibers, charcoal, as well as newly discovered nanocarbon materials, such as fullerene, graphene, carbon nanotube, and graphene nanoribbon (GNR). Even though all are composed of the same atoms, different carbon materials can show very different physical and chemical properties, including electrical transport, optical and thermal properties, and chemical reactivity, depending on their structures.

Electrochemistry has been connected to carbon materials since the early days of electrochemistry research [1], and the discoveries of new carbon materials in the past decades have been accompanied by research advances concerning the doping of these materials using electrochemical techniques, with an emphasis on materials preparation, characterization, and applications.

Among the electrochemical techniques and characterization tools, vibrational and optical spectroscopies have been important. Electrochemical charge transfer, an important process in electrochemistry, influences not only the electronic structure of the materials but also their vibrational and optical properties, which are all dependent on the concentration of electrons and holes found in the solid. Therefore, valuable data can be obtained when electrochemistry and *in situ* Raman spectroscopy are applied simultaneously under the heading of spectroelectrochemistry. Such investigations have been carried out extensively on carbon nanomaterials in order to investigate the effects of electron and hole doping.

One advantage of electrochemistry over other experimental techniques is its ability to introduce higher levels of dopants and to make quantitative, reproducible measurements [2, 3]. The electrochemical setup including the choice of the particular electrolyte is an important factor that influences the doping efficiency in spectroelectrochemical experiments. Different electrolytes can thereby require larger electrode potentials than others to achieve the same doping levels, so that attention needs to be given to the choice of the electrolyte for studying a given

Electrochemistry of Carbon Electrodes, First Edition.
Edited by Richard C. Alkire, Philip N. Bartlett and Jacek Lipkowski.

material system. Failures to pay attention to such issues have, in the past, led to apparent inconsistencies between different sets of published data.

The basic carbon material introduced in this chapter is graphene, which is a single layer of crystalline graphite, because it is the basic building block behind sp^2 carbon materials. Graphite, which represents nature's way to build up stacks of graphene layers into a bulk crystal, is then introduced briefly, together with the synthetic commercial product, highly oriented pyrolytic graphite (HOPG), which closely resembles graphite. Another commonly used nanocarbon material, carbon nanotube, is also discussed, which has deep scientific interest, and is also interesting along with its related carbon fiber analog for electrochemical commercial applications. Porous carbon is an sp^2 carbon material useful for applications requiring a huge surface area, and is also discussed briefly. Diamond, which is commonly a symbol of societal wealth and prestige, is gaining more and more scientific attention recently due to its extraordinary properties in electrochemistry, quantum physics, and biology, and has promising applications in all of these fields. Finally, brief mention is made of other sp^2 nanocarbon materials with significant current scientific interest, carbon nanoribbons and porous carbon, and these materials may someday find interest for electrochemical science and applications.

In this chapter, we will introduce some typical carbon materials that are widely studied in electrochemistry. Their properties, not restricted to their electrochemical properties, will be briefly described. Some characterization techniques, including spectroelectrochemistry, will be described when applied to selected carbon materials. A brief overview of the application of various carbon materials to electrochemistry will be included in this chapter, which will be concluded by an outlook to the future.

1.2 Different Forms of Carbon

1.2.1 Graphene

1.2.1.1 Optical Properties

It is widely established that graphene has numerous fascinating properties [4–9]. Though considered as a semimetal, graphene has unique electromagnetic/plasmonic effects compared to conventional noble metals [10, 11]. First, its plasma frequency in the long-wavelength limit is expressed as [12–15]

$$\omega_{p,G} = \sqrt{\frac{8E_F\sigma_{uni}q}{\hbar\varepsilon}},$$

where E_F is the Fermi energy of graphene, σ_{uni} is the universal optical conductivity of graphene and is independent of any material parameters: $\sigma_{uni} = \pi e^2/(2h)$ [16, 17], q is the unit charge, and ε is the permittivity. Note that the expression

of plasma frequency for graphene is very different from that for metals which is [18]

$$\omega_{\mathrm{p,M}} = \sqrt{\frac{2\pi n e^2 q}{\varepsilon m}},$$

where n is the carrier density in graphene and m is the carrier effective mass. We can see that $\omega_{\mathrm{p,G}} \propto E_{\mathrm{F}}^{1/2} \propto n^{1/4}$ and $\omega_{\mathrm{p,M}} \propto n^{1/2}$. Such a difference in the plasma frequencies between graphene and metals is due to the Dirac fermions in graphene, rather than to ordinary Schrödinger fermions in normal metals. The plasma frequency of graphene is in the terahertz range, which is 10^3 times lower than ω_{p} in metals, and which can be tuned through gating or doping [11, 19, 20], or by fabricating graphene ribbons with micron widths (see Figure 1.1), where ω_{p} is in the terahertz range. Here, ω_{p} differs with the ribbon widths and with the Fermi energy E_{F}, as shown in Figure 1.1. Second, single-layer graphene has a linear dispersion relation and a uniform 2.293% light absorption across a wide frequency range [11, 21–23], resulting from its Dirac-cone band structure and linear energy–momentum relation $E(k)$, as seen in Figure 1.2. Many works have studied the surface plasmonic properties of graphene or graphene ribbons, with different experimental techniques, including optical measurements, electron energy loss spectroscopy, angle-resolved photoemission spectroscopy, and surface tunneling spectroscopy [19, 20, 24–26], as further discussed in the cited references.

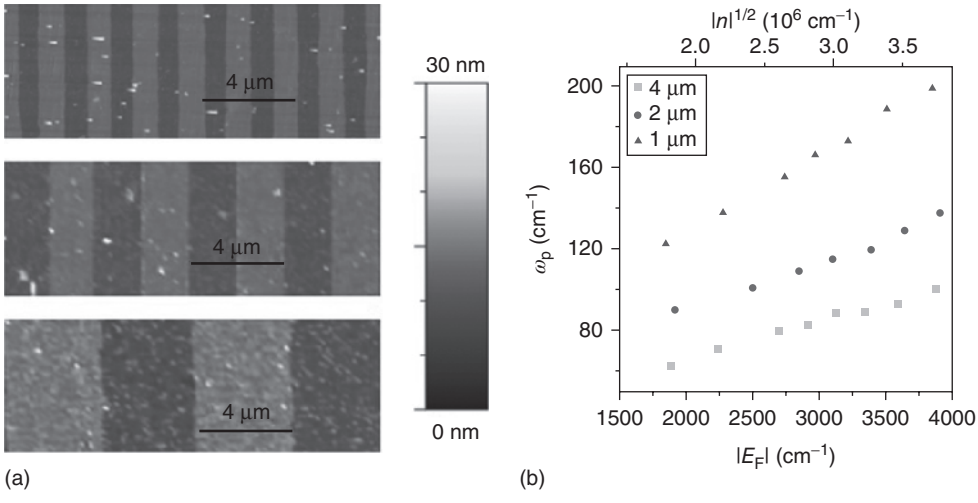

Figure 1.1 Control of the graphene plasmon resonance frequency by electrical gating and microribbon widths. (a) AFM (atomic force microscopy) images of graphene microribbons with widths of 1, 2, and 4 μm. Color bar of the height is shown on the right. (b) Fermi energy (E_{F}) dependence of the graphene plasmon frequency ω_{p} (top axis gives related dependence on charge density $|n|^{1/2}$) of ribbons with three different widths. (Figure adapted from Ref. [20].)

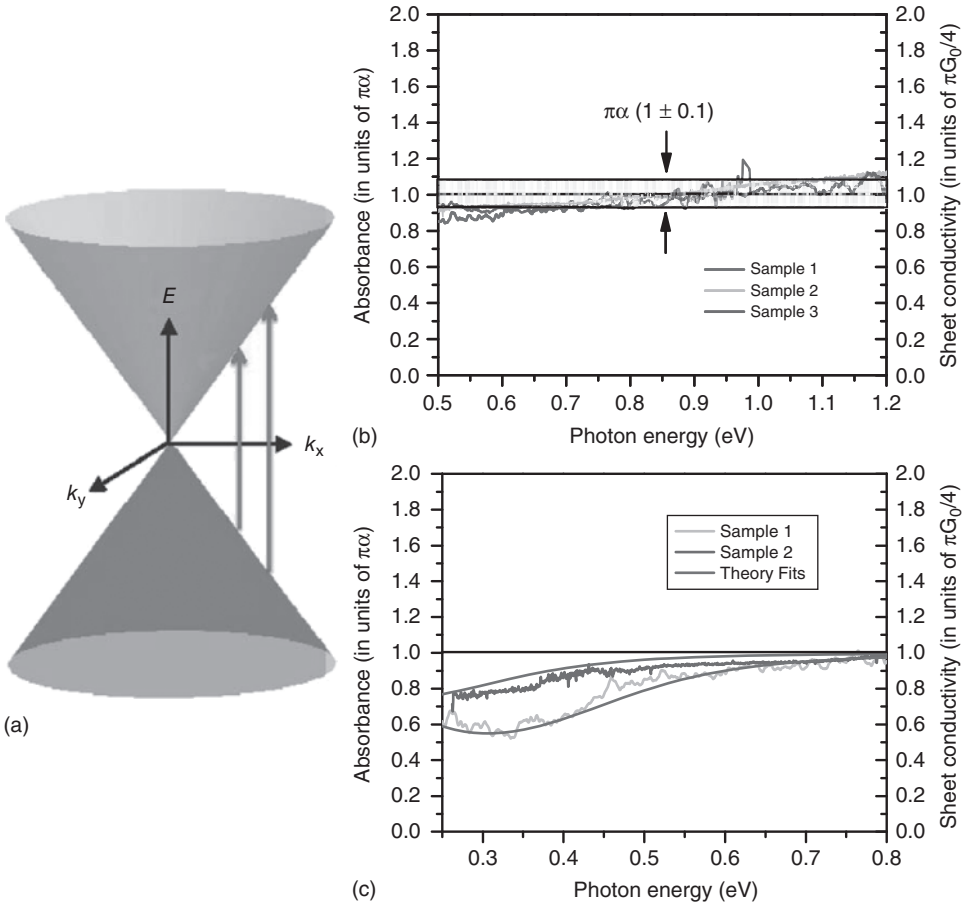

Figure 1.2 Universal light absorbance and optical conductivity of graphene. (a) Schematic of Dirac-cone and interband optical transitions in graphene. (b) Optical absorbance (left axis) and optical sheet conductivity (right axis) of three graphene samples. The spectral range is from 0.5 to 1.2 eV. The black horizontal line shows the universal absorbance value of 2.293% per layer, with the variation within 10%. (c) The optical absorbance of graphene Sample 1 and Sample 2 over a smaller spectral range from 0.25 to 0.8 eV. (Figure from Refs [22, 23].)

1.2.1.2 Electrical Properties and Tunability

One of the greatest advantages of studying graphene is that its transport and optical properties can be sensitively and controllably tuned by doping. The Fermi level can easily be shifted by introducing either electrons (n-doping) or holes (p-doping). Numerous ways of establishing a desired doping level have been investigated, for instance, by chemical doping [27, 28], electrochemical doping [29–33], electrostatically by top or back gating [34–36], and by the direct introduction of heteroatoms into the lattice [37].

One of the most studied and widely used techniques is to introduce the charge by top or back gating [34–36]. This technique is appealing due to its similarity to present use in gating field-effect transistors, which allows the knowledge and know-how learned from standard microelectronics to be used more widely in graphene electronics. However, one drawback of this approach is the extremely high gating potential (~100 V) that is required, because the present gate dielectrics have a relatively large thickness that restricts the gate capacitance value. For example, bias voltages as high as 80 V had to be used to achieve a carrier density of $\sim 5 \times 10^{12}$ cm^{-2} [36], and such a high bias voltage could cause charge trapping from the substrate, thereby altering the properties of both the substrate and the graphene.

Electrochemical doping, on the other hand, is significantly more efficient, insofar as voltages as small as 1.5 V are sufficient to reach charge carrier concentrations of 5×10^{13}cm^{-2}. Higher doping levels can also be achieved by using a combination of a protecting layer and a liquid electrolyte [3] or using ferroelectric polymers [38]. Electrochemical doping is thus especially appealing when higher doping levels are desired, and these high doping levels are achieved by the electrical double layer (EDL) formed at the interface between the electrolyte solution and the graphene surface. The ions in the liquid are attracted by the graphene, which is charged by an opposite sign. These ions migrate to the surface, thus forming a very thin layer that performs as a capacitor with an extremely high capacitance value. Therefore, effective control of carrier densities in the graphene can be implemented through electrochemistry, which furthermore provides a fast response by electrochemical doping.

1.2.1.3 **Spectroscopic Properties**

Spectroelectrochemical studies are most commonly carried out by using Raman spectroscopy, because this technique is readily available and does not normally perturb the material under investigation, thereby allowing repeated and systematic measurements. The commonly studied features in the Raman spectra of graphene are the G, D, and G′ bands (the G′ band is also called the 2D band), see Figure 1.3. The shapes of the electronic bands can be probed by varying the laser excitation energy, which shifts the peak position of the D and G′ bands and thus provides additional important information. Figure 1.4 shows the scattering processes that generate these vibrational bands or features [35]. From Figure 1.4, we can see that the G band comes from a first-order one-phonon scattering process, while other bands come from second-order scattering processes. The D band is a symmetry-breaking band, which thus requires the presence of defects in the sample, although boundaries (edges) of the sample also produce D band intensity. Since the D band is not allowed by the crystal symmetry of the graphene lattice, it is commonly used to evaluate the quality of a particular graphene sample. The G and G′ bands are present in all sp^2 carbon and graphene-related materials, and are symmetry-allowed. The intensity, frequency, and linewidth of these bands are dependent on several factors, such as strain and doping, the number of graphene layers, and the laser excitation energy. For example, the

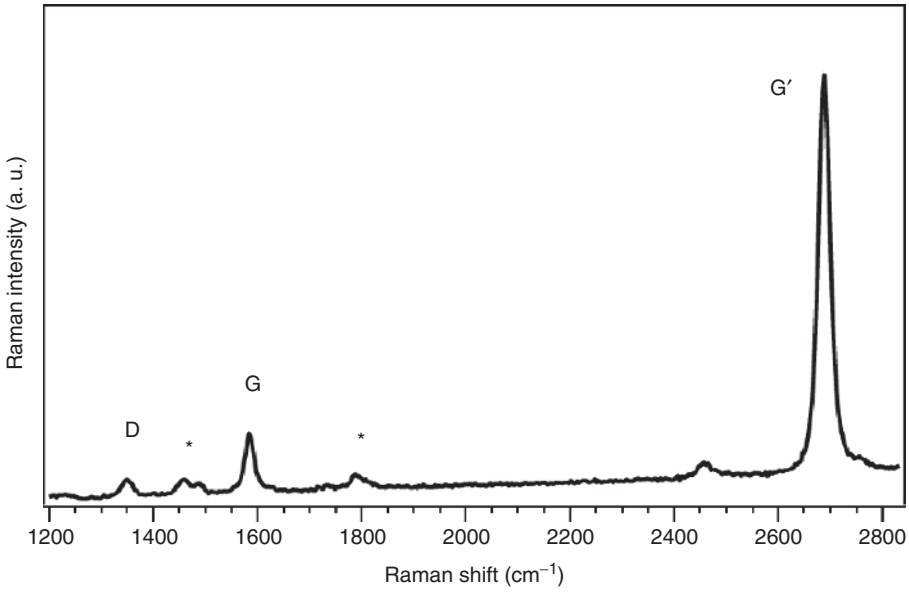

Figure 1.3 Raman spectrum of graphene at 0 V (applied bias voltage), excited by a 2.33 eV laser radiation, in an electrochemical environment. The asterisks (*) indicate Raman bands of the electrolyte. (From Ref. [33].)

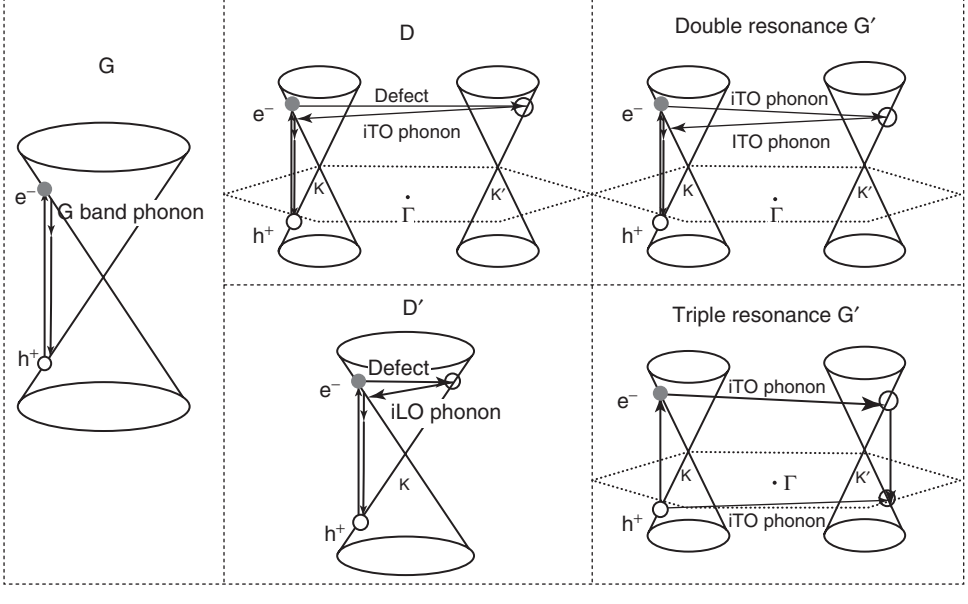

Figure 1.4 The Raman scattering processes of the G, D, D′, and G′ bands of graphene. (Figure is from Ref. [35].)

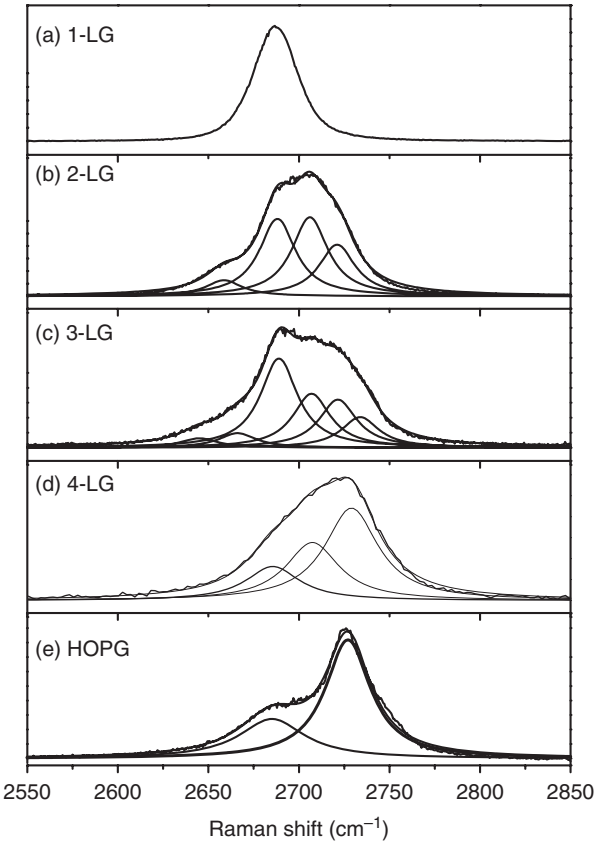

Figure 1.5 Raman spectra of the G′ band of graphene with different numbers of layers. The excitation laser wavelength is 514 nm. (Figure is from Ref. [35].)

shape of the G′ band of graphene is related to the number of graphene layers and how the layers are stacked with respect to one another. As shown in Figure 1.5 [35], the shape of the G′ band is dramatically different from single layer to four layers and to bulk HOPG (highly oriented pyrolytic graphite, discussed later). The G′ band is generated from the second-order two-phonon intervalley scattering process (Figure 1.4), and the G′ band can be fitted with multiple Lorentzian lineshapes, depending upon the structure of the sample.

The experimental setup of *in situ* Raman spectroelectrochemistry is shown in Figure 1.6 [39]. In the setup, the sample on the substrate serves as a working electrode and is surrounded by electrolyte solution (light grey cylinders). Note that the electrochemical setup requires a high-purity electrolyte, because the contaminants reduce the range of potential that can be applied. The sample is usually contacted by an Au metal (working electrode). The electrochemical cell is completed by an Ag pseudo-reference electrode and a Pt counterelectrode. The three-electrode system and potentiostatic control of the applied voltage assure

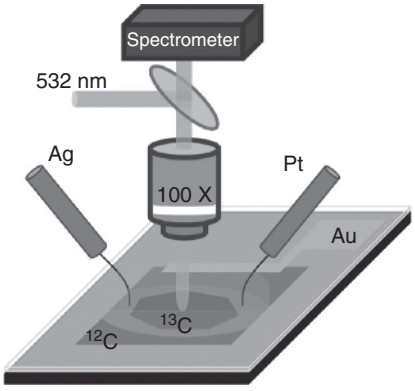

Figure 1.6 The schematic illustration of an experimental setup of *in situ* Raman spectroelectrochemistry. The sample (^{12}C/^{13}C bilayer graphene in this sketch) is on the substrate with ionic gating (light grey cylinders), with two electrode probes made of Ag and Pt. The back gating is through the Au metal electrode. The setup is placed under the Raman spectrometer to achieve *in situ* Raman spectroscopy. (Figure is from Ref. [39].)

precise control of the doping level of graphene. The electrochemical cell is placed under the Raman spectrometer to achieve *in situ* spectral acquisition. In Figure 1.6, the sample is a ^{12}C/^{13}C graphene bilayer, but only the ^{12}C part of the samples is contacted, which enables one to study the charge transfer between individual graphene layers in this system.

The doping of graphene results in changes in all Raman spectral features. These changes reflect variations in the electronic structure of graphene and the stress in the formation of defects. Hence, spectroelectrochemistry is a powerful tool to study charged graphene.

Using spectroelectrochemistry to accurately control and shift the Fermi level, it has, for example, been found that the intensity of the D peak decreases with increasing doping [40], as seen in Figure 1.7. Such an effect was attributed to the fact that the strength of the electron scattering is doping dependent, such that the total scattering rate of the photoexcited electrons and holes increases with doping. It is consequently important to know the doping level of the graphene when estimating the amount and type of defects from the intensity of the D peak.

The G band in Figure 1.3 is observed to be due to the optical phonon of graphene, which occurs at a high frequency of $\sim$1580 cm^{-1}, because the carbon atoms are very light, having atomic number 6. From a many-body point of view, the origin of the G band can be explained as that of an electron that is excited from the valence band into a conduction band by absorbing a phonon. An electron–hole pair is thus created. When the electron and the hole then recombine, a phonon is emitted, which has a slightly shifted frequency and a lifetime connected to its bandwidth. The energy of the phonon and the charge carriers

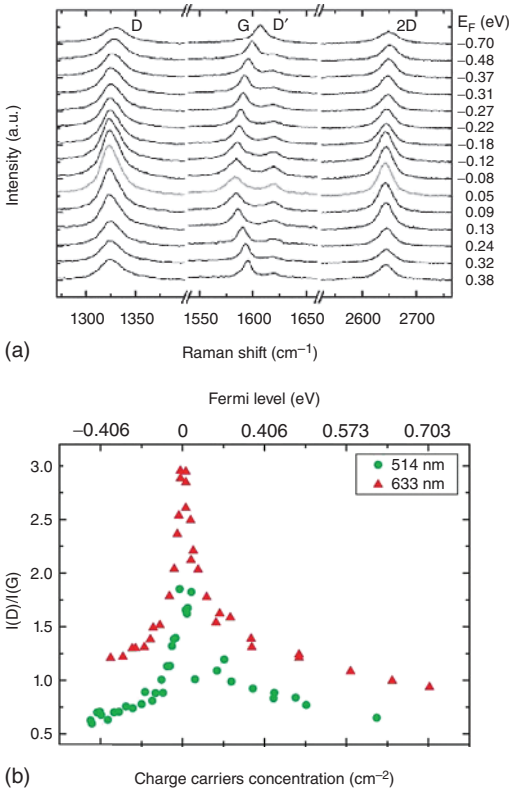

Figure 1.7 The change of D band with electrochemical doping. (a) Raman spectra of defective graphene at different Fermi energies (E_F), measured under 633 nm laser excitation. (b) The normalized intensity of the D band as a function of Fermi level, or charge carrier concentration at 514 and 633 nm laser excitations. (Figure is adapted from Ref. [40].)

will thus be renormalized by the various interactions. Since the band structure of graphene is conical with a linear $E(k)$ relation (see Figure 1.2a), and thereby symmetric for electrons and holes with respect to the Dirac point, the frequency shift of the G band upon doping can be expected to be equal for positive and negative doping. However, the C–C bond strength is also changed somewhat when the graphene is doped [36]. Positive (negative) charge doping removes (adds) electrons from (to) antibonding orbitals which increases (decreases) the bond strength. This phenomenon has an opposite effect on positive doping relative to negative doping, as seen in the electrochemical data shown in Figure 1.8. Both the renormalization and the bond strength change lead to an upshift of the phonon frequency for positive doping [29, 33]. For negative doping, on the other hand, the two effects work against each other [29, 33]. This results in a monotonic upshift of

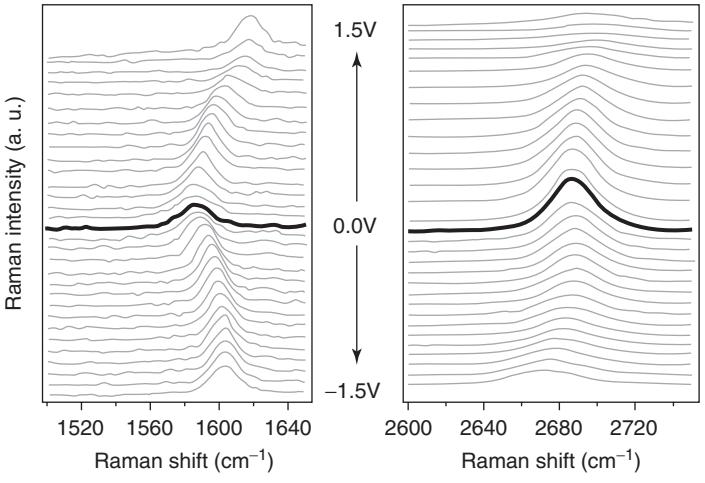

Figure 1.8 *In situ* Raman spectroelectrochemistry data for the G and G′ bands of graphene excited by 2.33 eV laser irradiation. The heavy black trace is for $V = 0$ applied voltage. (Adapted from Ref. [33].)

the G band frequency for positive doping and a nonmonotonic upshift for negative doping, whereby the shift is always greater for positive doping [33], as seen in Figure 1.8.

Another important effect that was observed in doped graphene samples was an anomalous increase of the intensity of the G mode at high electrode potentials [3, 33, 41]. This effect was explained by canceling part of possible optical transitions due to quantum interference effects [42].

The G′ or 2D band in Figure 1.3 is also sensitive to doping, although to a lesser extent than the G band, as is seen in Figure 1.8. Doping induces changes in the frequency of the G′ band due to changes in the C–C bond strength, the electron–phonon coupling, and electron–electron interactions. The frequency of the G′ band increases for positive doping, whereas it first increases for negative doping followed by a relatively large decrease at higher negative potentials. It has been found both experimentally [33] and theoretically [43] that the G band frequency shifts by ~0.5 times as much as the G′ band per volt in the range from 0 to 1 V. Strain can also influence the frequency of the G and G′ band. The two effects can be disentangled from one another by correlating the peak positions in the Raman spectra [33, 44].

The effect of doping on bi- [30] and trilayers [32] has been investigated by a combination of isotopic labeling with *in situ* Raman spectroelectrochemistry. The isotopic labeling allows separate investigation of the individual layers in the multilayered graphene, since the different masses of ^{12}C and ^{13}C result in a large difference of ω_G and $\omega_{G'}$ in the Raman spectra. A typical isotopically labeled turbostatic bilayer graphene sample has the Raman spectra shown in Figure 1.9. The isotope labeling also enables one to study the role of the stacking order of

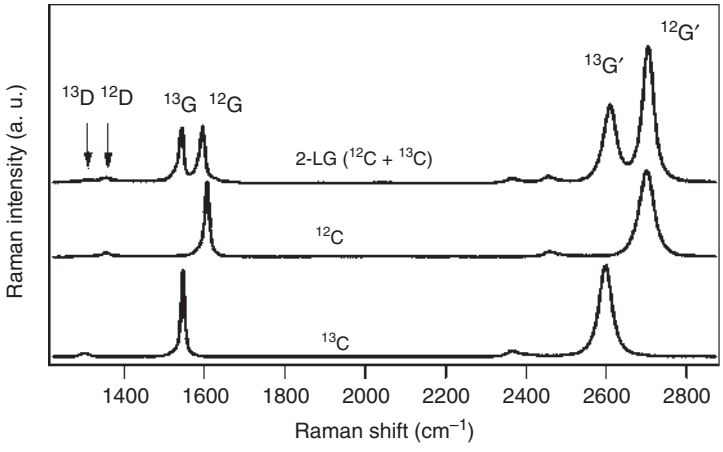

Figure 1.9 The Raman spectra of bilayer graphene with the two layers of: ^{13}C/^{12}C, both ^{13}C, and both ^{12}C. The graphene with the ^{13}C isotope has red-shifted G and G′ peaks, compared to ^{12}C graphene. (Figure from Ref. [30].)

graphene layers on the changes in electronic structure of graphene induced by doping [39]. A more complete review of the combination of isotopic labeling with *in situ* Raman spectroelectrochemistry is found in the review article by Frank *et al.* [31].

1.2.2 HOPG

Highly oriented pyrolytic graphite (HOPG) is a commonly used synthetic type of graphite with high purity and has an angular spread in the stacking of its graphite sheets of less than 1° [45]. The level of angular spread and perfection of HOPG can be characterized by the full-width half-maximum (FWHM) of the Cu-Kα rocking curve measured using X-ray diffraction (XRD). HOPG exhibits an anisotropy similar to graphite and is cleavable. Because of the anisotropy, many of its physical properties, including thermal, electrical, and optical properties [46], are different in different directions, as for example, along and perpendicular to the basal plane (Table 1.1). HOPG normally shows weak ferromagnetism due to the presence of magnetic impurities associated with the HOPG synthesis process. The observed magnetism is attributed to the unpaired electron spins at the grain boundaries and to the sample edges, and such effects have been characterized using magnetic force microscopy [48]. HOPG is a highly stable material and it remains stable at high temperatures (3000 °C under vacuum and 500 °C in atmosphere), and exhibits high chemical inertness to almost every chemical. Because of its atomically flat surface, HOPG is usually used as a calibration standard for scanning probe microscopy [49].

HOPG has also been widely used in the field of electrochemistry. The basal plane of HOPG has been used as electrodes for many studies, such as for the creation

Table 1.1 Physical properties of HOPG at 300 K [47].

	Along layer plane (002)	Along (0001) principal axis *c*
Electrical resistivity (Ω cm)	$3.5-5.0 \times 10^{-5}$	0.15–0.25
Thermal conductivity ($W\,m^{-1}\,K^{-1}$)	1700 ± 100	8 ± 1
Thermal expansion (K^{-1})	-1×10^{-6}	20×10^{-6}

of nanoscale interfaces for sensing and for biological applications [50, 51], as well as model system for nanoparticle electrocatalysis [52, 53], heterogeneous metal deposition, and nucleation studies [51, 54]. Besides, HOPG is commonly used to study the electrochemistry of sp^2 carbon materials used for improving our understanding of electrochemical processes, such as electrocatalysis [55] and carbon surface functionalization [56].

1.2.3 Carbon Nanotube

1.2.3.1 Structure and Electronic Properties

A carbon nanotube is a seamless 1D structure of rolled-up graphene [57]. Because of the dimensional constraints, the energy bands of a carbon nanotube become discrete [58–60], as shown in Figure 1.10. Moreover, the nanotube axis orientation relative to the six-member ring honeycomb lattice can vary from 0° to 30° (see Figure 1.11), rendering the classification of carbon nanotubes into zigzag ($\theta = 0°$), armchair ($\theta = 30°$), and chiral nanotubes, which are defined according to the nanotube profile along the diameter (perpendicular to nanotube axis). Sketches of these three types of carbon nanotubes are shown in Figure 1.12. Different types of carbon nanotubes have different electrical properties [57]. As shown in Figure 1.11

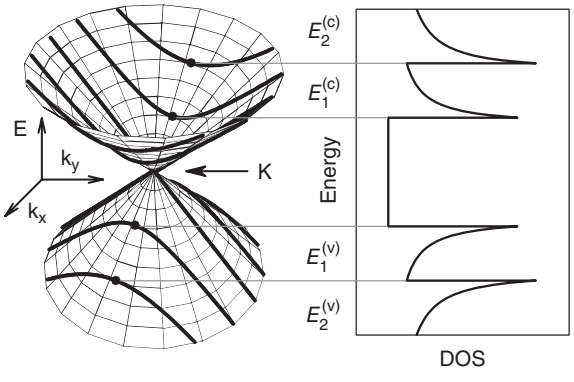

Figure 1.10 Energy band diagram and density of states (DOS) of a carbon nanotube. The 1D van Hove singularities give a high DOS at well-defined energies. (Figure adapted from Ref. [82].)

[60], the chirality of a carbon nanotube can be defined by the chiral vector $\vec{C}_h$, which can be written as [59]

$$\vec{C}_h = n\vec{a}_1 + m\vec{a}_2 \triangleq (n, m),$$

where $\vec{a}_1$ and $\vec{a}_2$ are the unit vectors of graphene. Different chiralities denoted by the indices (n, m) of carbon nanotubes (the orientation of the hexagons in Figure 1.11 relative to nanotube axis) distinguish between metallic and semiconducting types. Briefly, the condition for a metallic carbon nanotube is [59]

$$2n + m = 3j,$$

where j is an integer. This is also shown in Figure 1.11.

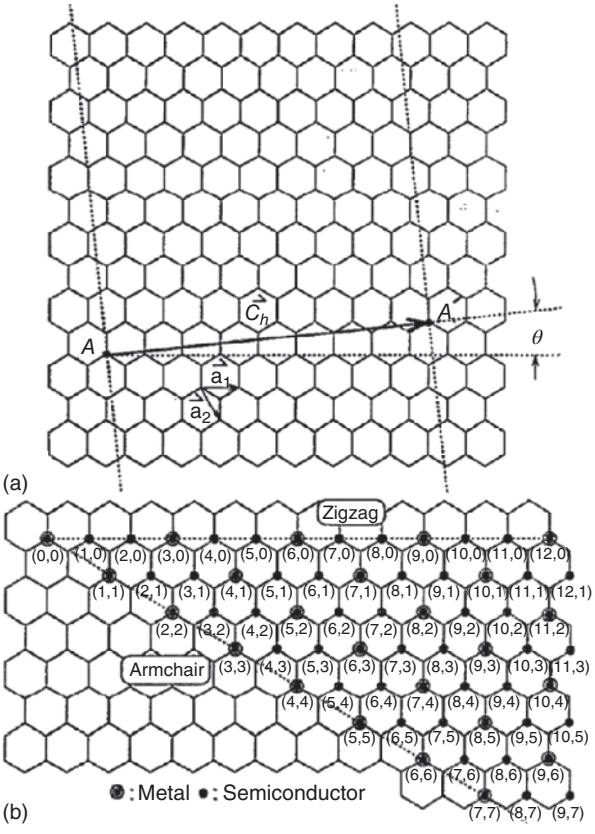

Figure 1.11 (a) A carbon nanotube defined by the chiral vector $\vec{C}_h$, which is perpendicular to the nanotube axis. Here, θ is the chiral angle, and $\vec{a}_1$ and $\vec{a}_2$ are the unit vectors of graphene. (b) Possible chiral vectors (n, m) of carbon nanotubes (see text). Different (n, m) chiralities result in different physical properties, including metallic (large dots) and semiconducting (small dots) nanotubes. (Figure adapted from Ref. [59].)

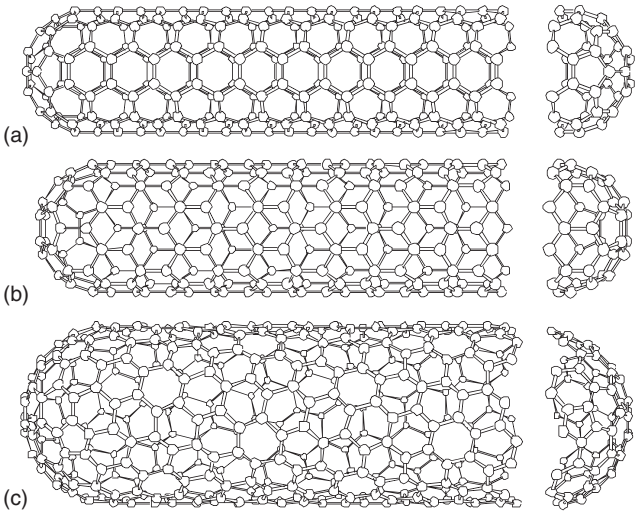

Figure 1.12 Three types of carbon nanotubes: (a) armchair, (b) zigzag, and (c) chiral. The definition of nanotube types is according to the orientation perpendicular to the nanotube axis. (Figure from Ref. [82].)

1.2.3.2 **Spectroscopy and Spectroelectrochemistry of Carbon Nanotubes**

The investigation of doped single-wall carbon nanotubes (SWCNTs) by Raman spectroscopy was first reported in 1997 by Rao *et al.* [61]. Even though this first report did not employ electrochemistry, it showed evidence of doping in the Raman spectra, which contributed to the observed frequency shifts of the G band. Electrochemistry connected with Raman spectroscopy has also been used to study the electron–phonon coupling and the charge states of nanotubes in solution or on substrates. The first study employing both electrochemistry and Raman spectroscopy on SWCNTs was published in 1999, by Eklund *et al.* [62]. The experiment also combined chemical and electrochemical doping, since the doping medium that was used, H_2SO_4, caused parallel chemical and electrochemical doping. Afterward, many other studies, employing numerous aqueous [63–68], and aprotic media (a solution that does not donate H^+ protons) [58, 69–79] followed.

Because a SWCNT is a graphene sheet rolled up seamlessly to form a tube, the Raman signature of carbon nanotubes also contains the D, G, and 2D bands, similar to the Raman spectrum of graphene, although with some differences. For instance, the curvature of the nanotube leads to a G band with two clear components, G^+ and G^-, assigned to transverse (TO) and longitudinal (LO) modes, vibrating along directions perpendicular (TO) or parallel (LO) to the nanotube axis, respectively. This situation is in contrast to graphene where these two modes are degenerate, since graphene is a quasi-2D material. This is shown in Figure 1.13. The G band lineshape, namely its LO component, is sensitive to the Fermi energy, and can be changed by applying a gate voltage. The LO mode exhibits different

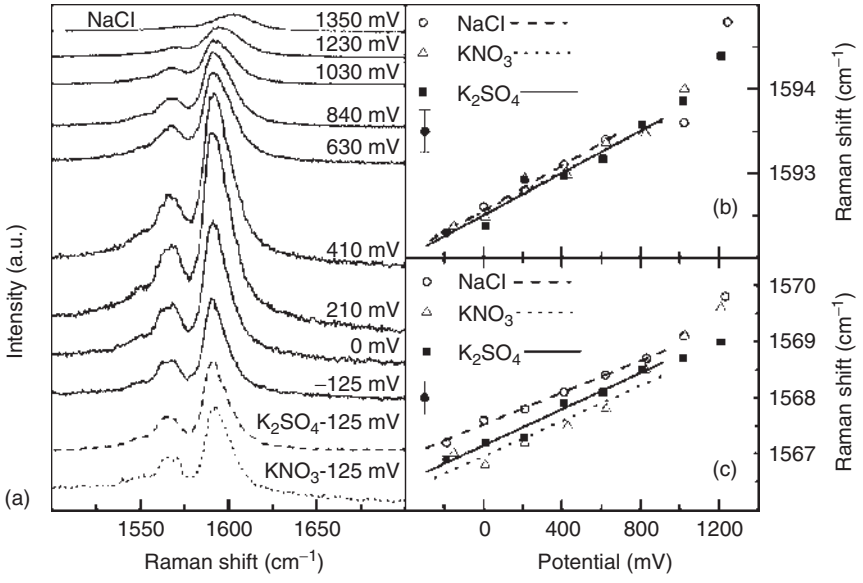

Figure 1.13 (a) Raman spectra of the G band at several potentials applied to a SWCNT bundle. (b,c) Variation of the G+ band and G− band frequency, respectively, with the applied potential for three different electrolyte solutions. (Adapted from Ref. [80].)

lineshapes depending upon whether the probed nanotube is metallic or semiconducting. For metallic nanotubes, the LO component exhibits a Kohn anomaly, which leads to a larger downshift of the peak frequency compared with semiconducting tubes [43].

In addition, the Raman spectrum of nanotubes shows a feature called the radial breathing mode (RBM) with a frequency ω_{RBM} between 100 and 350 cm^{-1}. The RBM mode is one of the most important features observed in the Raman spectrum of nanotubes, since it provides information regarding the nanotube diameter and the nanotube chirality, through the Kataura plot [81]. The Kataura plot shown in Figure 1.14 is a plot of the relationship between the electronic transition energies and the SWCNT diameters. Each point in the Kataura plot shows an optically allowed electronic transition energy, which is the energy separation between van Hove singularities in the conduction and valence bands. In Figure 1.14 [81–83], crosses represent semiconducting SWCNTs (labeled "S") and circles represent metallic SWCNTs (labeled "M"). For Raman spectroscopy, this plot gives information about the (n, m) SWCNT chiralities that can be excited for a certain laser excitation energy.

Raman spectroscopy can detect changes in the C–C bond length, since the RBM varies with diameter and the G band varies with the axial C–C bond length. Moreover, the band intensity also varies as charge transfer occurs, either to or from the nanotubes. Gupta *et al.* [84] monitored the dependence of the C–C bond length in an SWCNT material on charge transfer, for several alkali, halide, and sulfate

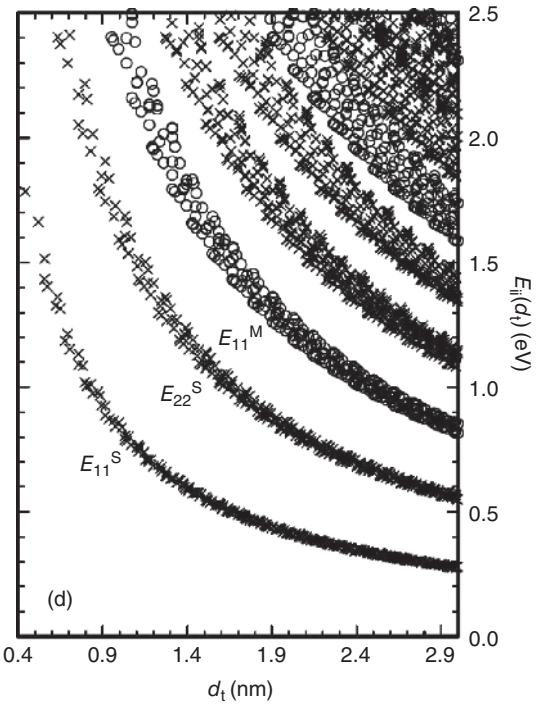

Figure 1.14 Kataura plot [81–83], showing the relationship between electronic transition energies and the SWCNT diameters. Each point on the plot shows an optically allowed electronic transition energy E_{ii}, which is the energy separation between van Hove singularities in the conduction band to the valence band. Crosses represent semiconducting SWCNTs (labeled "S") and circles represent metallic SWCNTs (labeled "M").

electrolyte solutions (see Figure 1.15), and observed a softening of the C–C bond with increasing charge transfer to the nanotubes.

SWCNT bundles containing nanotubes with different diameters are easy to obtain experimentally, but such samples may lead to overlapping RBM modes and complex Raman spectra that are difficult to interpret. In contrast, SWCNTs synthesized via the HiPCO method are favored for spectroelectrochemical studies due to their small diameters, which lead to well-separated RBM peaks, thereby simplifying nanotube chirality assignments significantly [58, 72].

The doping of SWCNT leads to changes in all Raman features. The most obvious effect is an overall bleaching of the Raman signal of carbon nanotubes. The shift of the Fermi level cancels the effect of the optical transitions between the van Hove singularities. If these transitions are employed in resonance effects, the Raman signal is dramatically reduced. The doping level, where the Raman signal starts to bleach, should therefore depend on the electronic structure of a particular carbon nanotube. It was indeed observed that the Raman signal of metallic tubes starts to bleach at a lower electrode potential than that of semiconducting tubes [70]. Moreover, a detailed spectroelectrochemical study of an individual

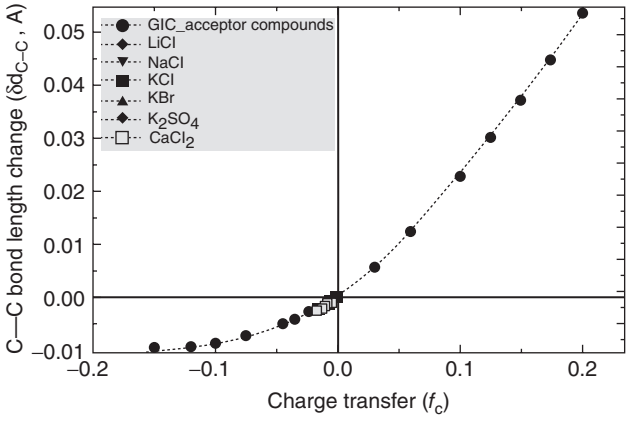

Figure 1.15 Variation of the C–C bond length (estimated from G band variation) with electrochemical charge transfer (f_c) induced on the nanotubes. (Adapted from Ref. [84].)

SWCNT showed that the "speed" of bleaching of the Raman signal also depends on the match of the nanotube resonance window and laser excitation energy [77]. It was also observed that bleaching of the Raman signal occurs already when the Fermi level crosses any van Hove singularity, even though this singularity is not employed in the resonance enhancement of the Raman signal [85].

The doping-induced changes in the intensity of the Raman signal of carbon nanotubes also have important consequences, that is, they can complicate the quantification of the amount of the particular SWCNT or the quantification of the defect density in SWCNTs, since the D mode intensity is also strongly affected by doping [86, 87].

The doping of carbon nanotubes also causes variations of the frequencies of the Raman features. These doping-induced changes are only subtle in SWCNTs in the case of RBM bands [74], but they are significant for the G and G′ modes [69, 73, 88]. The frequency variation of the G mode is rationalized by changes of the C–C bond strength and also changes in the phonon renormalization energy [71]. In the case of nanotube bundles, the changes in the G mode frequency of individual nanotubes contribute to the change of the G band lineshape of nanotube bundles [69, 89]. Nevertheless, the change in the G mode lineshape can be used to estimate the doping level of carbon nanotubes [69]. The changes in the G′ mode frequencies are quite complex even in the case of individual carbon nanotubes, and more detailed studies are needed to understand these phenomena [73].

The spectroelectrochemistry of double-wall carbon nanotubes (DWCNTs) has also been investigated [2, 90–97]. Nevertheless, the understanding of the effect of the doping is more difficult in DWCNTs. In general, the charge is located mostly on the outer tubes; hence, there is a difference between the doping level of the inner and outer tubes. The distinct doping effects for inner and outer tubes are observed in the RBM modes and in the D and G′ bands as well. For doped DWCNTs, both the D and G′ bands split into two components upon electrochemical

charging, in which case the mode at higher frequency is assigned to the outer tubes, since they bleach more rapidly [90, 91, 98]. These differences in the doping behavior can be used to distinguish between the Raman features of inner and outer tubes [94, 95] and even to quantify the amount of DWCNTs in their mixture with SWCNTs [2] in a given sample. Nevertheless, it should be noted that the charge distribution between the inner and outer tubes also strongly depends on their electronic structures, as shown in a recent study on sorted DWCNTs [96, 97].

Fullerene peapods represent another class of nanotube-based materials, which have been widely studied by spectroelectrochemistry [99–102]. The doping behavior of these materials is in general somewhat analogous to DWCNTs, but there are still some unexplained phenomena, such as the anomalous enhancement of the $A_g(2)$ mode of C_{60}@SWCNT at high anodic potentials [103]. Hence, further investigation of these materials is needed.

Spectroelectrochemistry has proven to provide a versatile technique in the field of nanocarbons. It allows the monitoring of the charge transfer to and from carbon nanotubes and graphene, inducing doping in a controlled and easy manner. In fact, spectroelectrochemistry also allows exploration of the possibility of unzipping SWCNTs of different chiralities to obtain GNRs [104]. Metallic nanotubes with smaller diameters were found to unzip at lower potentials (0.36 eV) than other SWCNTs, followed by metallic tubes with larger diameters (at 1.16 eV), while semiconducting nanotubes required even higher potentials (1.66 eV) to unzip [104].

1.2.4
Graphene Nanoribbon

A GNR is a quasi-1D nanomaterial derived from graphene. Like carbon nanotubes, GNRs also show distinct differences in physical properties between their armchair, zigzag, or chiral categories (Figure 1.16) [105], because GNRs have edges and are not rolled up seamlessly, as are carbon nanotubes. GNRs also have

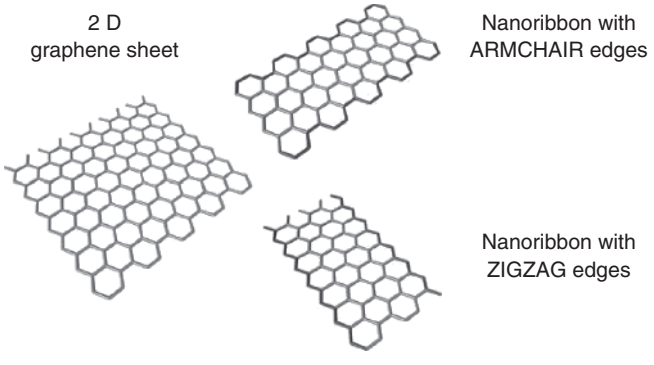

Figure 1.16 GNRs with different chiral orientations: zigzag and armchair. (Figure is from Ref. [105].)

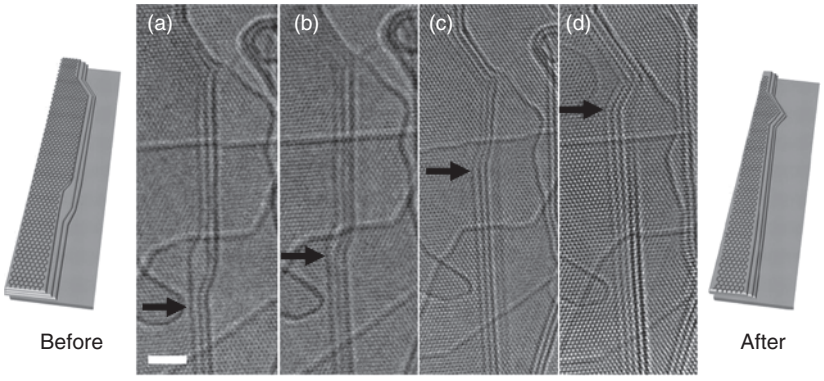

Figure 1.17 Development of edge structures in graphene nanoribbons using Joule heating inside a TEM (transmission electron microscope). (a) Graphene nanoribbon with zigzag–armchair edges. The black arrows indicate the junction between zigzag and armchair edges. With the increased time of Joule heating (a–d), the zigzag-armchair junction position moves. The sketches on the left and right of the TEM images (a–d) indicate the graphene nanoribbon structures before and after Joule heating, respectively. Scale bar in (a): 2 nm. (Figure from Ref. [109].)

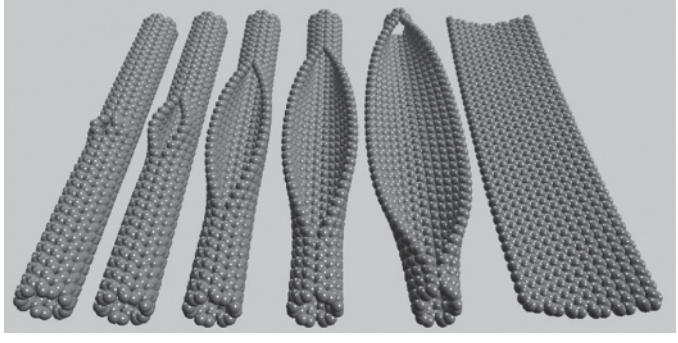

Figure 1.18 Unzipping a carbon nanotube to form a graphene nanoribbon. Figure from Ref. [110].

the distinctions of metallic or semiconducting types, due to the different axial or chiral orientations of their edges. Also, the band gaps of GNRs are decreased with increased ribbon width [106].

GNRs have high electron mobility, and small-width semiconducting GNRs have shown interesting band gaps, thus attracting the attention of electrical engineers for potential application in high-speed digital circuits. Because the electronic and magnetic properties of GNRs strongly depend on their edges [107, 108], the synthesis and precise control of GNR edge morphology have remained hot topics over the years. Potential precise synthesis techniques include *in situ* Joule heating inside a TEM (transmission electron microscope) [109] (Figure 1.17) and unzipping carbon nanotubes [110] (Figure 1.18), but practical large-scale applications

of these scientific demonstrations appear challenging at the present time. Moreover, due to their small width, GNRs have many dangling bonds on their edges, which influence their chemical properties. This characteristic of GNRs triggers scientific study of their electrochemical reactivity [111] and offers an attractive system to study electrochemical applications, such as for electrode materials in Li-ion batteries [112] and for molecule sensing [113].

1.2.5 Diamond

The electrochemistry of diamond is currently a rapidly growing field, because of the special properties of diamond, such as (i) extreme mechanical hardness, thereby providing an ideal material for ultrasound technology [114, 115], (ii) transparency over a wide spectral range, allowing optical applications [116, 117], (iii) biological compatibility, enabling its use in biological studies and medical applications [118, 119], (iv) apability to be doped to provide electrical conduction with tunable transport properties [120, 121], (v) very high thermal conductivity, allowing its use as a heat sink for electronic applications [122, 123], (vi) chemical inertness, making it ideal for application in harsh and corrosive environments [124, 125], as well as at high temperature and pressure, (vii) negative electron affinity making it a promising material for active devices, such as field-effect transistors [126, 127], and (viii) the quantum singlet–triplet spin states and N-V defect centers existing in nanodiamond, which open up chances to explore quantum information and quantum physics [128–132].

Highly boron-doped diamond films, which have been widely studied in electrochemistry, can be grown by chemical vapor deposition (CVD) and are electrically conductive. Different electrochemical properties of boron-doped diamond films have been studied, such as reactivity [133] and electronic structure [134]. Different characterization techniques have been used to study the electrochemistry of diamond, such as scanning electron microscopy [123, 135] and Raman spectroscopy [125, 136].

1.2.6 Porous Carbon

Porous carbons constitute a family of lightweight carbon materials with special properties. Porous carbon materials can be made through pyrolysis and by activation of carbonaceous precursors, showing adsorption volumes of 0.5–0.8 $cm^3\ g^{-1}$ and surface areas of 700–1800 $m^2\ g^{-1}$, depending upon the activation conditions and activation mechanisms [137]. These materials possess many micropores of varying sizes and thus can adsorb a large variety of molecules in large amounts. In fact, the application of porous carbon dates back to 2000 BCE in Egypt, when charcoals were used to purify water. Nowadays, porous carbons with more controllable micropore sizes and densities, also called *activated carbon*, have been made [138, 139], and well-developed internal surface area and porosity have been

achieved [140–142]. Nanocarbon materials, such as graphene, carbon nanotubes, and carbon nanofibers, have also been used as porous aerogels, because of their large surface areas [143–145], and have proven to be useful for applications as composites in supercapacitors, polymers, and energy storage.

1.3 Outlook

Different forms of carbons have different physical and chemical properties, but these different carbon forms are of interest in electrochemical studies and for many applications. Sufficient electrochemical research has already been done on carbon materials to demonstrate their importance in electrochemical energy storage, which is of societal importance. Various experimental techniques have been employed in conjunction with electrochemical methods to characterize carbon-based materials, such as Raman spectroscopy, scanning probe microscopy, electron microscopy, photoelectron spectroscopy, and others. Various manufacturing techniques have also been developed, for commercializing electrochemical carbon-based materials, especially in batteries for energy storage. In particular, nanocarbons, which have unique electrical, mechanical, optical, and chemical properties, have attracted the attention of electrochemists for both fundamental studies of their electrochemical properties and their exploration for future applications in batteries, electrodes, energy storage, environmental monitoring, and biological and medical science. The nanostructures developed in the last 30 years (carbon nanotubes and graphene) provide a great opportunity for both fundamental research and applications. The morphology of these materials strongly affects their electronic properties, and the recent experimental techniques allow one to monitor and control the nanostructure morphology to constantly increasing degrees, thereby providing a great potential for further research and applications.

In the following chapters of this textbook, different aspects of electrochemical research on carbon materials will be discussed in detail, including carbon electrodes in different applications (fuel cells, molecular electronics, sensing, etc.) using various methods (surface modification, carbon paste, carbon fiber, etc.), and electrochemistry of different carbon materials (graphene, HOPG, carbon nanotube, diamond, etc.).

References

1. Besenhard, J.O. and Fritz, H.P. (1983) The electrochemistry of black carbons. *Angew. Chem., Int. Ed. Engl.*, **22**(12), 950–975.
2. Kominkova, Z., Vales, V., Hersam, M.C., and Kalbac, M. (2014) Towards quantification of the ratio of the single and double wall carbon nanotubes in their mixtures: an in situ Raman spectroelectrochemical study. *Carbon N. Y.*, **78**, 366–373.
3. Kominkova, Z. and Kalbac, M. (2014) Extreme electrochemical doping of a graphene–polyelectrolyte heterostructure. *RSC Adv.*, **4**(22), 11311.

4. Geim, A.K. and Novoselov, K.S. (2007) The rise of graphene. *Nat. Mater.*, **6**(3), 183–191.
5. Nezich, D. and Palacios, T. (2009) Graphene frequency multipliers. *IEEE Electron Device Lett.*, **30**(5), 547–549.
6. Wang, H., Hsu, A., Wu, J., Kong, J., and Palacios, T. (2010) Graphene-based ambipolar RF mixers. *IEEE Electron Device Lett.*, **31**(9), 906–908.
7. Ci, L., Song, L., Jin, C., Jariwala, D., Wu, D., Li, Y., Srivastava, A., Wang, Z.F., Storr, K., Balicas, L., Liu, F., and Ajayan, P.M. (2010) Atomic layers of hybridized boron nitride and graphene domains. *Nat. Mater.*, **9**(5), 430–435.
8. Reddy, A.L.M., Srivastava, A., Gowda, S.R., Gullapalli, H., Dubey, M., and Ajayan, P.M. (2010) Synthesis of nitrogen-doped graphene films for lithium battery application. *ACS Nano*, **4**(11), 6337–6342.
9. Yoo, J.J., Balakrishnan, K., Huang, J., Meunier, V., Sumpter, B.G., Srivastava, A., Conway, M., Reddy, A.L.M., Yu, J., Vajtai, R., and Ajayan, P.M. (2011) Ultrathin planar graphene supercapacitors. *Nano Lett.*, **11**(4), 1423–1427.
10. Luo, X., Qiu, T., Lu, W., and Ni, Z. (2013) Plasmons in graphene: recent progress and applications. *Mater. Sci. Eng., R*, **74**(11), 351–376.
11. Grigorenko, A.N., Polini, M., and Novoselov, K.S. (2012) Graphene plasmonics. *Nat. Photonics*, **6**(11), 749–758.
12. Abedinpour, S.H., Vignale, G., Principi, A., Polini, M., Tse, W.-K., and MacDonald, A.H. (2011) Drude weight, plasmon dispersion, and ac conductivity in doped graphene sheets. *Phys. Rev. B*, **84**(4), 045429.
13. Polini, M., Asgari, R., Borghi, G., Barlas, Y., Pereg-Barnea, T., and MacDonald, A. (2008) Plasmons and the spectral function of graphene. *Phys. Rev. B*, **77**(8), 081411.
14. Hwang, E.H. and Das Sarma, S. (2007) Dielectric function, screening, and plasmons in two-dimensional graphene. *Phys. Rev. B*, **75**(20), 205418.
15. Wunsch, B., Stauber, T., Sols, F., and Guinea, F. (2006) Dynamical polarization of graphene at finite doping. *New J. Phys.*, **8**(12), 318–318.
16. Kuzmenko, A., van Heumen, E., Carbone, F., and van der Marel, D. (2008) Universal optical conductance of graphite. *Phys. Rev. Lett.*, **100**(11), 117401.
17. Nair, R.R., Blake, P., Grigorenko, A.N., Novoselov, K.S., Booth, T.J., Stauber, T., Peres, N.M.R., and Geim, A.K. (2008) Fine structure constant defines visual transparency of graphene. *Science*, **320**(5881), 1308.
18. Ashcroft, N.W. and Mermin, N.D. (1976) *Solid State Physics*, Cengage Learning.
19. Fei, Z., Rodin, A.S., Andreev, G.O., Bao, W., McLeod, A.S., Wagner, M., Zhang, L.M., Zhao, Z., Thiemens, M., Dominguez, G., Fogler, M.M., Castro Neto, A.H., Lau, C.N., Keilmann, F., and Basov, D.N. (2012) Gate-tuning of graphene plasmons revealed by infrared nano-imaging. *Nature*, **487**(7405), 82–85.
20. Ju, L., Geng, B., Horng, J., Girit, C., Martin, M., Hao, Z., Bechtel, H.A., Liang, X., Zettl, A., Shen, Y.R., and Wang, F. (2011) Graphene plasmonics for tunable terahertz metamaterials. *Nat. Nanotechnol.*, **6**(10), 630–634.
21. Bao, Q. and Loh, K.P. (2012) Graphene photonics, plasmonics, and broadband optoelectronic devices. *ACS Nano*, **6**(5), 3677–3694.
22. Mak, K.F., Sfeir, M.Y., Wu, Y., Lui, C.H., Misewich, J.A., and Heinz, T.F. (2008) Measurement of the optical conductivity of graphene. *Phys. Rev. Lett.*, **101**(19), 196405.
23. Mak, K.F., Ju, L., Wang, F., and Heinz, T.F. (2012) Optical spectroscopy of graphene: from the far infrared to the ultraviolet. *Solid State Commun.*, **152**(15), 1341–1349.
24. Eberlein, T., Bangert, U., Nair, R., Jones, R., Gass, M., Bleloch, A., Novoselov, K., Geim, A., and Briddon, P. (2008) Plasmon spectroscopy of free-standing graphene films. *Phys. Rev. B*, **77**(23), 233406.

25. Chen, J., Badioli, M., Alonso-González, P., Thongrattanasiri, S., Huth, F., Osmond, J., Spasenović, M., Centeno, A., Pesquera, A., Godignon, P., Elorza, A.Z., Camara, N., García de Abajo, F.J., Hillenbrand, R., and Koppens, F.H.L. (2012) Optical nano-imaging of gate-tunable graphene plasmons. *Nature*, **487**(7405), 77–81.
26. Yan, H., Li, X., Chandra, B., Tulevski, G., Wu, Y., Freitag, M., Zhu, W., Avouris, P., and Xia, F. (2012) Tunable infrared plasmonic devices using graphene/insulator stacks. *Nat. Nanotechnol.*, **7**(5), 330–334.
27. Jung, N., Kim, N., Jockusch, S., Turro, N.J., Kim, P., and Brus, L. (2009) Charge transfer chemical doping of few layer graphenes: charge distribution and band gap formation. *Nano Lett.*, **9**(12), 4133–4137.
28. Zhang, W., Lin, C.-T., Liu, K.-K., Tite, T., Su, C.-Y., Chang, C.-H., Lee, Y.-H., Chu, C.-W., Wei, K.-H., Kuo, J.-L., and Li, L.-J. (2011) Opening an electrical band gap of bilayer graphene with molecular doping. *ACS Nano*, **5**(9), 7517–7524.
29. Das, A., Pisana, S., Chakraborty, B., Piscanec, S., Saha, S.K., Waghmare, U.V., Novoselov, K.S., Krishnamurthy, H.R., Geim, A.K., Ferrari, A.C., and Sood, A.K. (2008) Monitoring dopants by Raman scattering in an electrochemically top-gated graphene transistor. *Nat. Nanotechnol.*, **3**(4), 210–215.
30. Kalbac, M., Farhat, H., Kong, J., Janda, P., Kavan, L., and Dresselhaus, M.S. (2011) Raman spectroscopy and in situ Raman spectroelectrochemistry of bilayer $^{12}C/^{13}C$ graphene. *Nano Lett.*, **11**(5), 1957–1963.
31. Frank, O., Dresselhaus, M.S., and Kalbac, M. (2015) Raman spectroscopy and in-situ Raman spectroelectrochemistry of isotopically engineered graphene systems. *Acc. Chem. Res.*, **48**(1), 111–118.
32. Kalbac, M., Kong, J., and Dresselhaus, M.S. (2012) Raman spectroscopy as a tool to address individual graphene layers in few-layer graphene. *J. Phys. Chem. C*, **116**(35), 19046–19050.
33. Kalbac, M., Reina-Cecco, A., Farhat, H., Kong, J., Kavan, L., and Dresselhaus, M.S. (2010) The influence of strong electron and hole doping on the Raman intensity of chemical vapor-deposition graphene. *ACS Nano*, **4**(10), 6055–6063.
34. Freitag, M., Steiner, M., Martin, Y., Perebeinos, V., Chen, Z., Tsang, J.C., and Avouris, P. (2009) Energy dissipation in graphene field-effect transistors. *Nano Lett.*, **9**(5), 1883–1888.
35. Malard, L.M., Pimenta, M.A., Dresselhaus, G., and Dresselhaus, M.S. (2009) Raman spectroscopy in graphene. *Phys. Rep.*, **473**(5-6), 51–87.
36. Yan, J., Zhang, Y., Kim, P., and Pinczuk, A. (2007) Electric field effect tuning of electron-phonon coupling in graphene. *Phys. Rev. Lett.*, **98**(16), 166802.
37. Meyer, J.C., Kurasch, S., Park, H.J., Skakalova, V., Künzel, D., Gross, A., Chuvilin, A., Algara-Siller, G., Roth, S., Iwasaki, T., Starke, U., Smet, J.H., and Kaiser, U. (2011) Experimental analysis of charge redistribution due to chemical bonding by high-resolution transmission electron microscopy. *Nat. Mater.*, **10**(3), 209–215.
38. Kalbac, M., Kong, J., and Dresselhaus, M.S. (2013) Doping of bi-layer graphene by gradually polarizing a ferroelectric polymer. *Phys. Status Solidi*, **250**(12), 2649–2652.
39. Araujo, P.T., Frank, O., Mafra, D.L., Fang, W., Kong, J., Dresselhaus, M.S., and Kalbac, M. (2013) Mass-related inversion symmetry breaking and phonon self-energy renormalization in isotopically labeled AB-stacked bilayer graphene. *Sci. Rep.*, **3**, 2061.
40. Bruna, M., Ott, A.K., Ijäs, M., Yoon, D., Sassi, U., and Ferrari, A.C. (2014) Doping dependence of the Raman spectrum of defected graphene. *ACS Nano*, **8**(7), 7432–7441.
41. Chen, C.-F., Park, C.-H., Boudouris, B.W., Horng, J., Geng, B., Girit, C., Zettl, A., Crommie, M.F., Segalman, R.A., Louie, S.G., and Wang, F. (2011) Controlling inelastic light scattering quantum pathways in graphene. *Nature*, **471**(7340), 617–620.

42. Basko, D.M. (2009) Calculation of the Raman G peak intensity in monolayer graphene: role of Ward identities. *New J. Phys.*, **11**(9), 095011.
43. Piscanec, S., Lazzeri, M., Mauri, F., Ferrari, A., and Robertson, J. (2004) Kohn anomalies and electron-phonon interactions in Graphite. *Phys. Rev. Lett.*, **93**(18), 185503.
44. Lee, J.E., Ahn, G., Shim, J., Lee, Y.S., and Ryu, S. (2012) Optical separation of mechanical strain from charge doping in graphene. *Nat. Commun.*, **3**, 1024.
45. Moore, R.R., Banks, C.E., and Compton, R.G. (2004) Basal plane pyrolytic graphite modified electrodes: comparison of carbon nanotubes and graphite powder as electrocatalysts. *Anal. Chem.*, **76**(10), 2677–2682.
46. Zanini, M., Grubisic, D., and Fischer, J.E. (1978) Optical anisotropy of highly oriented pyrolytic graphite. Effect of surface preparation. *Phys. Status Solidi*, **90**(1), 151–156.
47. McNaught, A.D. and Wilkinson, A. (1997) *Compendium of Chemical Terminology: IUPAC Recommendations*, Blackwell Science, p. 450.
48. Červenka, J., Katsnelson, M.I., and Flipse, C.F.J. (2009) Room-temperature ferromagnetism in graphite driven by two-dimensional networks of point defects. *Nat. Phys.*, **5**(11), 840–844.
49. Lapshin, R.V. (1998) Automatic lateral calibration of tunneling microscope scanners. *Rev. Sci. Instrum.*, **69**(9), 3268.
50. Liu, H., Favier, F., Ng, K., Zach, M.P., and Penner, R.M. (2001) Size-selective electrodeposition of meso-scale metal particles: a general method. *Electrochim. Acta*, **47**(5), 671–677.
51. Menke, E.J., Li, Q., and Penner, R.M. (2004) Bismuth telluride (Bi2Te3) nanowires synthesized by cyclic electrodeposition/stripping coupled with step edge decoration. *Nano Lett.*, **4**(10), 2009–2014.
52. González Orive, A., Grumelli, D., Vericat, C., Ramallo-López, J.M., Giovanetti, L., Benitez, G., Azcárate, J.C., Corthey, G., Fonticelli, M.H., Requejo, F.G., Hernández Creus, A., and Salvarezza, R.C. (2011) 'Naked' gold nanoparticles supported on HOPG: melanin functionalization and catalytic activity. *Nanoscale*, **3**(4), 1708–1716.
53. Brülle, T. and Stimming, U. (2009) Platinum nanostructured HOPG – preparation, characterization and reactivity. *J. Electroanal. Chem.*, **636**(1–2), 10–17.
54. Zach, M.P., Inazu, K., Ng, K.H., Hemminger, J.C., and Penner, R.M. (2002) Synthesis of molybdenum nanowires with millimeter-scale lengths using electrochemical step edge decoration. *Chem. Mater.*, **14**(7), 3206–3216.
55. Crevillen, A.G., Pumera, M., Gonzalez, M.C., and Escarpa, A. (2009) The preferential electrocatalytic behaviour of graphite and multiwalled carbon nanotubes on enediol groups and their analytical implications in real domains. *Analyst*, **134**(4), 657–662.
56. Jouikov, V. and Simonet, J. (2012) Novel method for grafting alkyl chains onto glassy carbon. Application to the easy immobilization of ferrocene used as redox probe. *Langmuir*, **28**(1), 931–938.
57. Saito, R., Dresselhaus, M.S., and Dresselhaus, G. (1998) *Physical Properties of Carbon Nanotubes*, Imperial College Press, p. 259.
58. Kavan, L., Kalbac, M., Zukalova, M., and Dunsch, L. (2005) Electrochemical doping of chirality-resolved carbon nanotubes. *J. Phys. Chem. B*, **109**(42), 19613–19619.
59. Saito, R., Fujita, M., Dresselhaus, G., and Dresselhaus, M.S. (1992) Electronic structure of chiral graphene tubules. *Appl. Phys. Lett.*, **60**(18), 2204.
60. Liu, C.-H. and Zhang, H.-L. (2010) Chemical approaches towards single-species single-walled carbon nanotubes. *Nanoscale*, **2**(10), 1901–1918.
61. Rao, A.M., Eklund, P.C., Bandow, S., Thess, A., and Smalley, R.E. (1997) Evidence for charge transfer in doped carbon nanotube bundles from. *Raman Scattering*, **388**(6639), 257–259.
62. Sumanasekera, G.U., Allen, J.L., Fang, S.L., Loper, A.L., Rao, A.M., and Eklund, P.C. (1999) Electrochemical

oxidation of single wall carbon nanotube bundles in sulfuric acid. *J. Phys. Chem. B*, **103**(21), 4292–4297.

63. An, C.P., Vardeny, Z.V., Iqbal, Z., Spinks, G., Baughman, R.H., and Zakhidov, A. (2001) Raman scattering study of electrochemically doped single wall nanotubes. *Synth. Met.*, **116**(1–3), 411–414.
64. Corio, P., Jorio, A., Demir, N., and Dresselhaus, M.S. (2004) Spectroelectrochemical studies of single wall carbon nanotubes films. *Chem. Phys. Lett.*, **392**(4-6), 396–402.
65. Cronin, S.B., Barnett, R., Tinkham, M., Chou, S.G., Rabin, O., Dresselhaus, M.S., Swan, A.K., Ünlü, M.S., and Goldberg, B.B. (2004) Electrochemical gating of individual single-wall carbon nanotubes observed by electron transport measurements and resonant Raman spectroscopy. *Appl. Phys. Lett.*, **84**(12), 2052.
66. Gupta, S. (2011) Ion transport and electrochemical tuning of Fermi level in single-wall carbon nanotubes: In situ Raman scattering. *J. Mater. Res.*, **22**(03), 603–614.
67. Rafailov, P., Maultzsch, J., Thomsen, C., and Kataura, H. (2005) Electrochemical switching of the Peierls-like transition in metallic single-walled carbon nanotubes. *Phys. Rev. B*, **72**(4), 045411.
68. Wang, Z., Pedrosa, H., Krauss, T., and Rothberg, L. (2006) Determination of the exciton binding energy in single-walled carbon nanotubes. *Phys. Rev. Lett.*, **96**(4), 047403.
69. Kalbac, M., Kavan, L., Dunsch, L., and Dresselhaus, M.S. (2008) Development of the tangential mode in the Raman spectra of SWCNT bundles during electrochemical charging. *Nano Lett.*, **8**, 1257–1264.
70. Kalbac, M., Kavan, L., and Dunsch, L. (2008) Changes in the electronic states of single walled carbon nanotubes as followed by a Raman spectroelectrochemical analysis of the radial breathing mode. *J. Phys. Chem. C*, **112**(43), 16759–16763.
71. Kalbac, M., Farhat, H., Kavan, L., Kong, J., and Dresselhaus, M.S. (2008) Competition of a spring force constant and a phonon energy renormalization in electrochemically doped semiconducting single walled carbon nanotubes. *Nano Lett.*, **8**(10), 3532–3537.
72. Kavan, L. and Dunsch, L. (2003) Diameter-selective electrochemical doping of hipco single-walled carbon nanotubes. *Nano Lett.*, **3**(7), 969–972.
73. Kalbac, M., Kavan, L., Farhat, H., Kong, J., and Dresselhaus, M.S. (2009) A large variety of behaviors for the Raman G′ mode of single wall carbon nanotubes upon electrochemical gating arising from different (n,m) of individual nanotubes. *J. Phys. Chem. C*, **113**(5), 1751–1757.
74. Farhat, H., Sasaki, K., Kalbac, M., Hofmann, M., Saito, R., Dresselhaus, M.S., and Kong, J. (2009) Softening of the radial breathing mode in metallic carbon nanotubes. *Phys. Rev. Lett.*, **102**, 126804.
75. Kalbac, M. and Kavan, L. (2010) The influence of doping on the Raman intensity of the D band in single walled carbon nanotubes. *Carbon N. Y.*, **48**, 832–838.
76. Kalbac, M., Kavan, L., Zukalová, M., and Dunsch, L. (2006) The intermediate frequency modes of single- and double-walled carbon nanotubes: a Raman spectroscopic and in situ Raman spectroelectrochemical study. *Chemistry*, **12**(16), 4451–4457.
77. Kalbac, M., Farhat, H., Kavan, L., Kong, J., Sasaki, K., Saito, R., and Dresselhaus, M. (2009) Electrochemical charging of individual single-walled carbon nanotubes. *ACS Nano*, **3**(8), 2320–2328.
78. Kalbác, M., Kavan, L., Zukalová, M., and Dunsch, L. (2006) The identification of dispersive and non-dispersive intermediate frequency modes of HiPco single walled carbon nanotubes by in situ Raman spectroelectrochemistry. *Phys. Status Solidi*, **243**, 3134–3137.
79. Kavan, L., Kalbác, M., Zukalová, M., and Dunsch, L. (2006) Raman spectroelectrochemistry of index-identified metallic carbon nanotubes: the resonance rule revisited. *Phys. Status Solidi*, **243**, 3130–3133.

80. Stoll, M., Rafailov, P.M., Frenzel, W., and Thomsen, C. (2003) Electrochemical and Raman measurements on single-walled carbon nanotubes. *Chem. Phys. Lett.*, **375**(5-6), 625–631.
81. Kataura, H., Kumazawa, Y., Maniwa, Y., Umezu, I., Suzuki, S., Ohtsuka, Y., and Achiba, Y. (1999) Optical properties of single-wall carbon nanotubes. *Synth. Met.*, **103**(1-3), 2555–2558.
82. Jorio, A., Saito, R., Dresselhaus, G., and Dresselhaus, M.S. (2011) *Raman Spectroscopy in Graphene Related Systems*, Wiley-VCH Verlag GmbH, Weinheim.
83. Kataura, H., Kumazawa, Y., Kojima, N., Maniwa, Y., Umezu, I., Masubuchi, S., Kazama, S., Zhao, X., Ando, Y., Ohtsuka, Y., Suzuki, S., and Achiba, Y. (1999) *Electronic Properties of Novel Materials*, AIP Conference Proceedings, vol. **486**, American Institute of Physics, Woodbury, NY, pp. 328–332.
84. Gupta, S., Hughes, M., Windle, A.H., and Robertson, J. (2004) In situ Raman spectro-electrochemistry study of single-wall carbon nanotube mat. *Diamond Relat. Mater.*, **13**(4-8), 1314–1321.
85. Kalbac, M. and Kavan, L. (2009) The influence of the resonant electronic transition on the intensity of the Raman radial breathing mode of single walled carbon nanotubes during electrochemical charging. *J. Phys. Chem. C*, **113**, 16408–16413.
86. Kalbac, M. and Kavan, L. (2010) Evaluation of defects concentration in doped SWCNT. *Phys. Status Solidi*, **247**, 2797–2800.
87. Kalbac, M., Hsieh, Y.-P., Farhat, H., Kavan, L., Hofmann, M., Kong, J., and Dresselhaus, M.S. (2010) Defects in individual semiconducting single wall carbon nanotubes: Raman spectroscopic and in situ Raman spectroelectrochemical study. *Nano Lett.*, **10**(11), 4619–4626.
88. Kalbac, M., Kavan, L., and Dunsch, L. (2009) In situ Raman spectroelectrochemistry of SWCNT bundles: development of the tangential mode during electrochemical charging in different electrolyte solutions. *Diamond Relat. Mater.*, **18**(5-8), 972–974.
89. Kalbac, M., Kavan, L., and Dunsch, L. (2009) The effect of bundling on the tangential displacement mode in the Raman spectra of semiconducting single walled carbon nanotubes during electrochemical charging. *J. Phys. Chem. C*, **113**(4), 1340–1345.
90. Kalbac, M., Kavan, L., Zukalova, M., and Dunsch, L. (2005) In-situ vis-near-infrared and Raman spectroelectrochemistry of double-walled carbon nanotubes. *Adv. Funct. Mater.*, **15**(3), 418–426.
91. Kavan, L., Kalbác, M., Zukalová, M., Krause, M., and Dunsch, L. (2004) Electrochemical doping of double-walled carbon nanotubes: an in situ Raman spectroelectrochemical study. *ChemPhysChem*, **5**(2), 274–277.
92. Kim, Y.A., Kojima, M., Muramatsu, H., Umemoto, S., Watanabe, T., Yoshida, K., Sato, K., Ikeda, T., Hayashi, T., Endo, M., Terrones, M., and Dresselhaus, M.S. (2006) In situ Raman study on single- and double-walled carbon nanotubes as a function of lithium insertion. *Small*, **2**(5), 667–676.
93. Pumera, M. (2007) Electrochemical properties of double wall carbon nanotube electrodes. *Nanoscale Res. Lett.*, **2**(2), 87–93.
94. Kalbác, M., Kavan, L., Zukalová, M., and Dunsch, L. (2007) The in situ Raman spectroelectrochemical study of 13C labeled fullerene peapods and double walled carbon nanotubes. *Small*, **3**, 1746–1752.
95. Kalbác, M., Kavan, L., and Dunsch, L. (2007) In situ Raman spectroelectrochemistry as a tool for the differentiation of inner tubes of DWCNT and thin SWCNT. *Anal. Chem.*, **79**, 9074–9081.
96. Kalbac, M., Green, A.A., Hersam, M.C., and Kavan, L. (2010) Tuning of sorted double-walled carbon nanotubes by electrochemical charging. *ACS Nano*, **4**(1), 459–469.
97. Kalbac, M., Green, A.A., Hersam, M.C., and Kavan, L. (2011) Probing charge transfer between shells of double-walled carbon nanotubes sorted by outer-wall electronic type. *Chem. Eur. J.*, **17**, 9806–9815.

98. Kalbác, M., Kavan, L., Zukalová, M., and Dunsch, L. (2004) Electrochemical tuning of high energy phonon branches of double wall carbon nanotubes. *Carbon N. Y.*, **42**(14), 2915–2920.
99. Kavan, L., Kalbac, M., Zukalova, M., Krause, M., Kataura, H., and Dunsch, L. (2005) Redox doping of double-wall carbon nanotubes and C60 peapods. *Fullerenes Nanotubes Carbon Nanostruct.*, **13**, 115–119.
100. Kavan, L., Kalbác, M., Zukalová, M., and Dunsch, L. (2006) Electrochemical and chemical redox doping of fullerene (C60) peapods. *Carbon N. Y.*, **44**, 99–106.
101. Kalbác, M., Kavan, L., Zukalová, M., and Dunsch, L. (2007) The influence of an extended fullerene cage: a study of chemical and electrochemical doping of C70 peapods by in situ Raman spectroelectrochemistry. *J. Phys. Chem. C*, **111**, 1079–1085.
102. Kalbác, M., Kavan, L., Zukalová, M., Yang, S., Cech, J., Roth, S., and Dunsch, L. (2007) The change of the state of an endohedral fullerene by encapsulation into SWCNT: a Raman spectroelectrochemical study of Dy3N@C80 peapods. *Chem. A Eur. J.*, **13**, 8811–8817.
103. Kalbac, M., Zólyomi, V., Rusznyák, Á., Koltai, J., Kürti, J., and Kavan, L. (2010) An anomalous enhancement of the Ag(2) mode in the resonance Raman spectra of C60 embedded in single walled carbon nanotubes during anodic charging. *J. Phys. Chem. C*, **114**, 2505–2511.
104. John, R., Shinde, D.B., Liu, L., Ding, F., Xu, Z., Vijayan, C., Pillai, V.K., and Pradeep, T. (2014) Sequential electrochemical unzipping of single-walled carbon nanotubes to graphene ribbons revealed by in situ Raman spectroscopy and imaging. *ACS Nano*, **8**(1), 234–242.
105. Jia, X., Campos-Delgado, J., Terrones, M., Meunier, V., and Dresselhaus, M.S. (2011) Graphene edges: a review of their fabrication and characterization. *Nanoscale*, **3**(1), 86–95.
106. Son, Y.-W., Cohen, M.L., and Louie, S.G. (2006) Half-metallic graphene nanoribbons. *Nature*, **444**(7117), 347–349.
107. Enoki, T., Kobayashi, Y., and Fukui, K.-I. (2007) Electronic structures of graphene edges and nanographene. *Int. Rev. Phys. Chem.*, **26**(4), 609–645.
108. Nakada, K., Fujita, M., Dresselhaus, G., and Dresselhaus, M. (1996) Edge state in graphene ribbons: nanometer size effect and edge shape dependence. *Phys. Rev. B*, **54**(24), 17954–17961.
109. Jia, X., Hofmann, M., Meunier, V., Sumpter, B.G., Campos-Delgado, J., Romo-Herrera, J.M., Son, H., Hsieh, Y.-P., Reina, A., Kong, J., Terrones, M., and Dresselhaus, M.S. (2009) Controlled formation of sharp zigzag and armchair edges in graphitic nanoribbons. *Science*, **323**(5922), 1701–1705.
110. Kosynkin, D.V., Higginbotham, A.L., Sinitskii, A., Lomeda, J.R., Dimiev, A., Price, B.K., and Tour, J.M. (2009) Longitudinal unzipping of carbon nanotubes to form graphene nanoribbons. *Nature*, **458**(7240), 872–876.
111. Jiang, D., Sumpter, B.G., and Dai, S. (2007) Unique chemical reactivity of a graphene nanoribbon's zigzag edge. *J. Chem. Phys.*, **126**(13), 134701.
112. Bhardwaj, T., Antic, A., Pavan, B., Barone, V., and Fahlman, B.D. (2010) Enhanced electrochemical lithium storage by graphene nanoribbons. *J. Am. Chem. Soc.*, **132**(36), 12556–12558.
113. Martín, A., Hernández-Ferrer, J., Vázquez, L., Martínez, M.-T., and Escarpa, A. (2014) Controlled chemistry of tailored graphene nanoribbons for electrochemistry: a rational approach to optimizing molecule detection. *RSC Adv.*, **4**(1), 132.
114. Wadhawan, J.D., Del Campo, F.J., Compton, R.G., Foord, J.S., Marken, F., Bull, S.D., Davies, S.G., Walton, D.J., and Ryley, S. (2001) Emulsion electrosynthesis in the presence of power ultrasound Biphasic Kolbe coupling processes at platinum and boron-doped diamond electrodes. *J. Electroanal. Chem.*, **507**(1-2), 135–143.
115. de Vidales, M.J.M., Barba, S., Sáez, C., Cañizares, P., and Rodrigo, M.A. (2014) Coupling ultraviolet light and ultrasound irradiation with conductive-diamond electrochemical oxidation

for the removal of progesterone. *Electrochim. Acta*, **140**, 20–26.

116. Zak, J.K., Butler, J.E., and Swain, G.M. (2001) Diamond optically transparent electrodes: demonstration of concept with ferri/ferrocyanide and methyl viologen. *Anal. Chem.*, **73**(5), 908–914.
117. Lin, C.-R., Liao, W.-H., Wei, D.-H., Shen, Y.-R., Chen, C.-L., Dong, C.-L., and Fang, W.-C. (2013) Fabrication of highly transparent ultrananocrystalline diamond films from focused microwave plasma jets. *Surf. Coat. Technol.*, **231**, 594–598.
118. Marken, F., Paddon, C.A., and Asogan, D. (2002) Direct cytochrome c electrochemistry at boron-doped diamond electrodes. *Electrochem. Commun.*, **4**(1), 62–66.
119. Prokop, A., Iwasaki, Y., and Harada, A. (eds) (2014) *Intracellular Delivery II*, vol. **7**, Springer, Dordrecht.
120. Davis, R.F. (1994) Deposition and characterization of diamond, silicon carbide and gallium nitride thin films. *J. Cryst. Growth*, **137**(1–2), 161–169.
121. Pernot, J., Volpe, P.N., Omnès, F., Muret, P., Mortet, V., Haenen, K., and Teraji, T. (2010) Hall hole mobility in boron-doped homoepitaxial diamond. *Phys. Rev. B*, **81**(20), 205203.
122. Twitchen, D.J., Pickles, C.S.J., Coe, S.E., Sussmann, R.S., and Hall, C.E. (2001) Thermal conductivity measurements on CVD diamond. *Diamond Relat. Mater.*, **10**(3-7), 731–735.
123. Schubert, T., Ciupiński, Ł., Zieliński, W., Michalski, A., Weißgärber, T., and Kieback, B. (2008) Interfacial characterization of Cu/diamond composites prepared by powder metallurgy for heat sink applications. *Scr. Mater.*, **58**(4), 263–266.
124. Lee, J., Tryk, D.A., Fujishima, A., and Park, S.-M. (2002) Electrochemical generation of ferrate in acidic media at boron-doped diamond electrodes. *Chem. Commun.*, **5**, 486–487.
125. Živcová, Z.V., Frank, O., Petrák, V., Tarábková, H., Vacík, J., Nesládek, M., and Kavan, L. (2013) Electrochemistry and in situ Raman spectroelectrochemistry of low and high quality boron doped diamond layers in aqueous electrolyte solution. *Electrochim. Acta*, **87**, 518–525.
126. Piantanida, G., Breskin, A., Chechik, R., Katz, O., Laikhtman, A., Hoffman, A., and Coluzza, C. (2001) Effect of moderate heating on the negative electron affinity and photoyield of air-exposed hydrogen-terminated chemical vapor deposited diamond. *J. Appl. Phys.*, **89**(12), 8259.
127. Yamaguchi, H., Masuzawa, T., Nozue, S., Kudo, Y., Saito, I., Koe, J., Kudo, M., Yamada, T., Takakuwa, Y., and Okano, K. (2009) Electron emission from conduction band of diamond with negative electron affinity. *Phys. Rev. B*, **80**(16), 165321.
128. Gaebel, T., Domhan, M., Popa, I., Wittmann, C., Neumann, P., Jelezko, F., Rabeau, J.R., Stavrias, N., Greentree, A.D., Prawer, S., Meijer, J., Twamley, J., Hemmer, P.R., and Wrachtrup, J. (2006) Room-temperature coherent coupling of single spins in diamond. *Nat. Phys.*, **2**(6), 408–413.
129. Balasubramanian, G., Neumann, P., Twitchen, D., Markham, M., Kolesov, R., Mizuochi, N., Isoya, J., Achard, J., Beck, J., Tissler, J., Jacques, V., Hemmer, P.R., Jelezko, F., and Wrachtrup, J. (2009) Ultralong spin coherence time in isotopically engineered diamond. *Nat. Mater.*, **8**(5), 383–387.
130. Lenef, A. and Rand, S. (1996) Electronic structure of the N-V center in diamond: theory. *Phys. Rev. B*, **53**(20), 13441–13455.
131. Kurtsiefer, C., Mayer, S., Zarda, P., and Weinfurter, H. (2000) Stable solid-state source of single photons. *Phys. Rev. Lett.*, **85**(2), 290–293.
132. Wrachtrup, J. and Jelezko, F. (2006) Processing quantum information in diamond. *J. Phys. Condens. Matter*, **18**(21), S807–S824.
133. Marken, F., Bhambra, A.S., Kim, D.-H., Mortimer, R.J., and Stott, S.J. (2004) Electrochemical reactivity of TiO2 nanoparticles adsorbed onto boron-doped diamond surfaces. *Electrochem. Commun.*, **6**(11), 1153–1158.

134. Liu, F.B., Wang, J.D., Liu, B., Li, X.M., and Chen, D.R. (2007) Effect of electronic structures on electrochemical behaviors of surface-terminated boron-doped diamond film electrodes. *Diamond Relat. Mater.*, **16**(3), 454–460.

135. Kromka, A., Rezek, B., Remes, Z., Michalka, M., Ledinsky, M., Zemek, J., Potmesil, J., and Vanecek, M. (2008) Formation of continuous nanocrystalline diamond layers on glass and silicon at low temperatures. *Chem. Vap. Deposition*, **14**(7-8), 181–186.

136. Patten, H.V., Meadows, K.E., Hutton, L.A., Iacobini, J.G., Battistel, D., McKelvey, K., Colburn, A.W., Newton, M.E., Macpherson, J.V., and Unwin, P.R. (2012) Electrochemical mapping reveals direct correlation between heterogeneous electron-transfer kinetics and local density of states in diamond electrodes. *Angew. Chem. Int. Ed.*, **51**(28), 7002–7006.

137. Lee, J., Kim, J., and Hyeon, T. (2006) Recent progress in the synthesis of porous carbon materials. *Adv. Mater.*, **18**(16), 2073–2094.

138. Gupta, V.K., Gupta, B., Rastogi, A., Agarwal, S., and Nayak, A. (2011) A comparative investigation on adsorption performances of mesoporous activated carbon prepared from waste rubber tire and activated carbon for a hazardous azo dye—Acid Blue 113. *J. Hazard. Mater.*, **186**(1), 891–901.

139. Li, L., Quinlivan, P.A., and Knappe, D.R.U. (2002) Effects of activated carbon surface chemistry and pore structure on the adsorption of organic contaminants from aqueous solution. *Carbon N. Y.*, **40**(12), 2085–2100.

140. Dutta, S., Bhaumik, A., and Wu, K.C.-W. (2014) Hierarchically porous carbon derived from polymers and biomass: effect of interconnected pores on energy applications. *Energy Environ. Sci.*, **7**(11), 3574–3592.

141. Chen, L.-F., Zhang, X.-D., Liang, H.-W., Kong, M., Guan, Q.-F., Chen, P., Wu, Z.-Y., and Yu, S.-H. (2012) Synthesis of nitrogen-doped porous carbon nanofibers as an efficient electrode material for supercapacitors. *ACS Nano*, **6**(8), 7092–7102.

142. Gong, Y., Wei, Z., Wang, J., Zhang, P., Li, H., and Wang, Y. (2014) Design and fabrication of hierarchically porous carbon with a template-free method. *Sci. Rep.*, **4**, 6349.

143. Worsley, M.A., Satcher, J.H., and Baumann, T.F. (2008) Synthesis and characterization of monolithic carbon aerogel nanocomposites containing double-walled carbon nanotubes. *Langmuir*, **24**(17), 9763–9766.

144. Horikawa, T., Hayashi, J., and Muroyama, K. (2004) Size control and characterization of spherical carbon aerogel particles from resorcinol–formaldehyde resin. *Carbon N. Y.*, **42**(1), 169–175.

145. Worsley, M.A., Pauzauskie, P.J., Olson, T.Y., Biener, J., Satcher, J.H., and Baumann, T.F. (2010) Synthesis of graphene aerogel with high electrical conductivity. *J. Am. Chem. Soc.*, **132**(40), 14067–14069.